Properties of Tropical Convection Observed by Millimeter-Wave Radar Systems

Graeme L. Stephens and Norman B. Wood

Department of Atmospheric Science, Colorado State University, Fort Collins, Colorado

ABSTRACT

This paper describes the results of analysis of over 825 000 profiles of millimeter-wave radar (MWR) reflectivities primarily collected by zenith-pointing surface radars observing tropical convection associated with various phases of activity of the large-scale tropical circulation. The data principally analyzed in this paper come from surface observations obtained at the Atmospheric Radiation Measurement Manus site during active and break episodes of the Madden–Julian oscillation (MJO) and from observations collected from a shipborne radar during an active phase of the monsoon over the Indian Ocean during the Joint Air–Sea Monsoon Interaction Experiment. It was shown, for example, in a histogram regime analysis that the MWR data produce statistics on convection regimes similar in most respects to the analogous regime analysis of the Tropical Rainfall Measuring Mission radar–radiometer observations. Attenuation of the surface MWRs by heavy precipitation, however, incorrectly shifts a small fraction of the deeper precipitation modes into the shallow modes of precipitation. The principal findings are the following. (i) The cloud and precipitation structures of the different convective regimes are largely identical regardless of the mode of synoptic forcing, that is, regardless of whether the convection occurred during an active phase of the MJO, a transition phase of the MJO, or in an active monsoon period. What changes between these synoptically forced modes of convection are the relative frequencies of occurrences of the different storm regimes. (ii) The cloud structures associated with the majority of cases of observed precipitation (ranging in occurrence from 45% to 53% of all precipitation profiles) were multilayered structures regardless of the mode of synoptic forcing. The predominant multilayered cloud mode was of higher-level cirrus of varying thickness overlying cumulus congestus–like convection. (iii) The majority of water accumulated (i.e., 53%–63%) over each of the periods assigned to the active monsoon (5 days of data), the active MJO (38 days of data), and the transition MJO (53 days of data) fell from these multiple-layered cloud systems. (iv) Solar transmittances reveal that significantly less sunlight (reductions of about 30%–50%) reaches the surface in the precipitating regimes than reaches the surface under drizzle and cloud-only conditions, suggesting that the optical thicknesses of precipitation-bearing clouds significantly exceeds those of nonprecipitating clouds.

---

1. Introduction

Cumulus convection is essential to many important interactions of the physical climate system (Arakawa 2004) and to the feedback mechanisms that modulate it (Stephens 2005). For example, most of the precipitation of global models derives from the cumulus parameterization scheme of these models. Furthermore, the dominant contribution of modeled water and temperature budgets of the free atmosphere, at least in the model Tropics, are from the convection schemes (e.g., Yao and Del Genio 1999) and model biases in these regions are most likely a consequence of cumulus convection parameterization errors.

Representing cumulus convection in global models and accounting for the interactions that are involved with convection has been a long-standing challenge to the modeling community (Arakawa 2004). Given the seminal role of convection in the climate system, it would therefore seem reasonable to expect that the parameterization methods developed to treat convection be tested thoroughly against all possible relevant observations. Such tests are also particularly important as convection parameterization schemes are highly sensitive to key parameters and crude assumptions about, for instance, microphysics (e.g., Emanuel and Zivkovic-Rothman 1999; Del Genio et al. 2005).

Aside from assessing the bulk effects of convection on the gross atmospheric budgets of moisture and tem-

Corresponding author address: Graeme L. Stephens, Department of Atmospheric Science, Colorado State University, Fort Collins, CO 80523-1371.
E-mail: stephens@atmos.colostate.edu

perature, detailed tests of convection schemes, especially in terms of other properties critical to the climate system, are largely absent from the literature (Johnson 1995; Emanuel and Zivkovic-Rothman 1999). Developing a strategy to compare details of these schemes with observations has also proven difficult, partly because convection parameterizations are formulated in terms of parameters that have not been adequately observed and partly because the schemes contain little direct information about those parameters that are more directly observable and important to climate, like cloud distributions (e.g., Bony and Emanuel 2001; Johnson 1995). More recently, cloud-resolving models (CRMs) have become important tools in the study of convection (e.g., Redelsperger et al. 2000) with these models even replacing the convection parameterizations in global models (e.g., Randall et al. 2003). However, detailed evaluation of CRMs is also in an unsatisfactory state being complicated, in part, by the sensitivity of these models to the imposed large-scale forcing (e.g., Benedetti et al. 2003b).

Although the current paper does not directly address the important problem of the evaluation of cumulus convection parameterization per se, it attempts to provide a rudimentary beginning to this topic. The paper describes analysis of observational data sources that, on the one hand, seem valuable for this purpose yet, on the other hand, have not traditionally been used in any real study of moist convection. The paper reviews a collection of observations of tropical convection gathered as a result of a number of measurement campaigns conducted over the past decade. The principal observations analyzed in this paper are derived from millimeter-wave radar (MWR) systems primarily in the form of MWR reflectivities. As such, the focus of this study differs from past MWR observational studies that mostly focus on layered cloud types and the effects of these clouds on radiation, as in MWR studies of cirrus (e.g., Mace et al. 1997) and stratocumulus (e.g., Frisch et al. 1995). MWRs are also beginning to emerge as valuable tools for studying precipitation. Analysis of the Doppler spectra measured from MWRs, especially when combined with other radar systems, offers great potential for studying the microphysics and kinematics of convective and stratiform precipitation (e.g., Kollias et al. 2003; Lhermitte 1988). MWR observations are also valuable for studying lighter rain and drizzle, such as observed in the East Pacific Investigation of Climate and the Dynamics and Chemistry of Marine Stratocumulus experiments (Bretherton et al. 2004; Stevens et al. 2003) as well as observing snow.

The essential purpose of this paper is to (i) document and characterize the MWR properties of tropical con-

vection and its cloudiness, (ii) compare the MWR properties of convection to those observed from the space-borne precipitation radar (PR) of the National Aeronautics and Space Administration (NASA) Tropical Rainfall Measurement Mission (TRMM; Kummerow et al. 2000), and (iii) relate the regimes evident in the MWR observations to other properties of convection. The significance of the convective regimes so identified on the broader tropical climate is beyond the immediate scope of this particular paper and is to be pursued in follow-up studies.

In the section to follow, the broad characteristics of MWR radar observations are briefly reviewed and it is shown how, for tropical cloud systems, MWR observations of the convective column of atmosphere from above are much less affected by the attenuation than for zenith-pointing surface-based radars, the consequence being that classification methods are also much less affected. This has obvious implications to analysis of the space-borne cloud radar data available from the CloudSat mission (Stephens et al. 2002). Despite the adverse effects of attenuation on surface MWRs, the relative frequency of total attenuation of MWRs in tropical convection is demonstrated to be small. Section 3 reviews the various sources of MWR data on tropical convection analyzed in this paper providing bulk statistical properties of the convection so observed. Two main sources of data that provide the bulk of the focus of the paper are the radar data collected from the Department of Energy (DOE) Atmospheric Radiation Measurement (ARM) site of Manus and the MWR data collected during a monsoon experiment in 1999. Section 4 introduces a method for identifying the occurrences of precipitation from MWR reflectivity profiles. Section 5 presents results from a comparative analysis of the TRMM PR and MWR precipitation data and subsequent interpretation of these data. The analysis presented uses an objective clustering method that is applied to both TRMM and the millimeter wavelength cloud radar (MMCR) data organized into two-dimensional histograms as introduced by Masunaga et al. (2005). Section 6 presents composite analysis of "storm classes" and includes properties of cloudiness differentiated by the occurrence of surface precipitation and the lack of precipitation. A surprising finding of the analysis presented in section 6 is that the storm classes considered earlier to be associated with the stratiform and deep convective modes of precipitation are in fact dominated by multilayered cloud structures with the bulk of the precipitation (more than 50% of the total mass that falls from all storm classes) derived from a type of congestus convection that occurs under thicker layers of cirrus. This result has many implica-

tions, a few of which are discussed in the final summary section.

2. Millimeter-wave radar observations

MWRs are able to penetrate optically thick cloud layers of high water content, yet detect optically thin cirrus clouds of low water content (e.g., Kropfli et al. 1995; Clothiaux et al. 1995). This feature makes them ideal tools for studying clouds and hence these radars are often referred to as "cloud" radars. Consequently, the relation between MWR scattering and cloud properties, notably the water and ice contents of clouds, has received much attention over the past decade or so especially with the advent of the MMCR in the ARM program (Moran et al. 1998) and the various activities associated with the CloudSat program (e.g., Stephens et al. 2002). Several methods exist to convert the measured radar reflectivities into cloud water and ice mass using either radar data alone (e.g., Liao and Sassen 1994) or radar data in combination with other measurements (Matrosov 1999; Austin and Stephens 2001; Mace et al. 1998; Benedetti et al. 2003a). More limited in number are studies that estimate precipitation microphysics and water content using MWR measurements (e.g., Kollias et al. 1999, 2003; Lhermitte 1988; L'Ecuyer and Stephens 2002; Matrosov 2005).

The MWRs used to study clouds operate at frequencies located either in the Ka-band, typically at wavelengths at 8 mm, or in the W-band frequency range near wavelengths of 3 mm. At these shorter wavelengths in particular, scattering from larger particles including precipitation often occurs in the so-called Mie regime[1] making the interpretation inherently ambiguous as scattering asymptotes to the geometric optics limit. Radars operating at millimeter wavelengths also suffer attenuation most notably by water vapor and precipitation and less so by cloud water (Stephens et al. 2002). As a consequence of these perceived complications, MWR measurements of precipitating cloud systems have received relatively little emphasis.

Although the attenuation of pulses of MWR is undesirable, useful methods exist to correct for attenuation given information about the path-integrated at-

---

[1] This nomenclature, used widely by the meteorological radar community, is strictly inaccurate (e.g., Stephens 1994). The Rayleigh scattering regime is characterized by $x = 2\pi r/\lambda \ll 1$ where r is the particle size and λ is the wavelength of the incident radiation. The scattering by particles in this regime systematically increase with x in a manner distinct from the regime $\gg 1$ in which the scattering properties gradually become invariant as x increases. The latter is more accurately referred to as the geometric optics limit but is commonly and inaccurately termed the Mie regime. In actual fact the Mie regime encompasses scattering for all x.
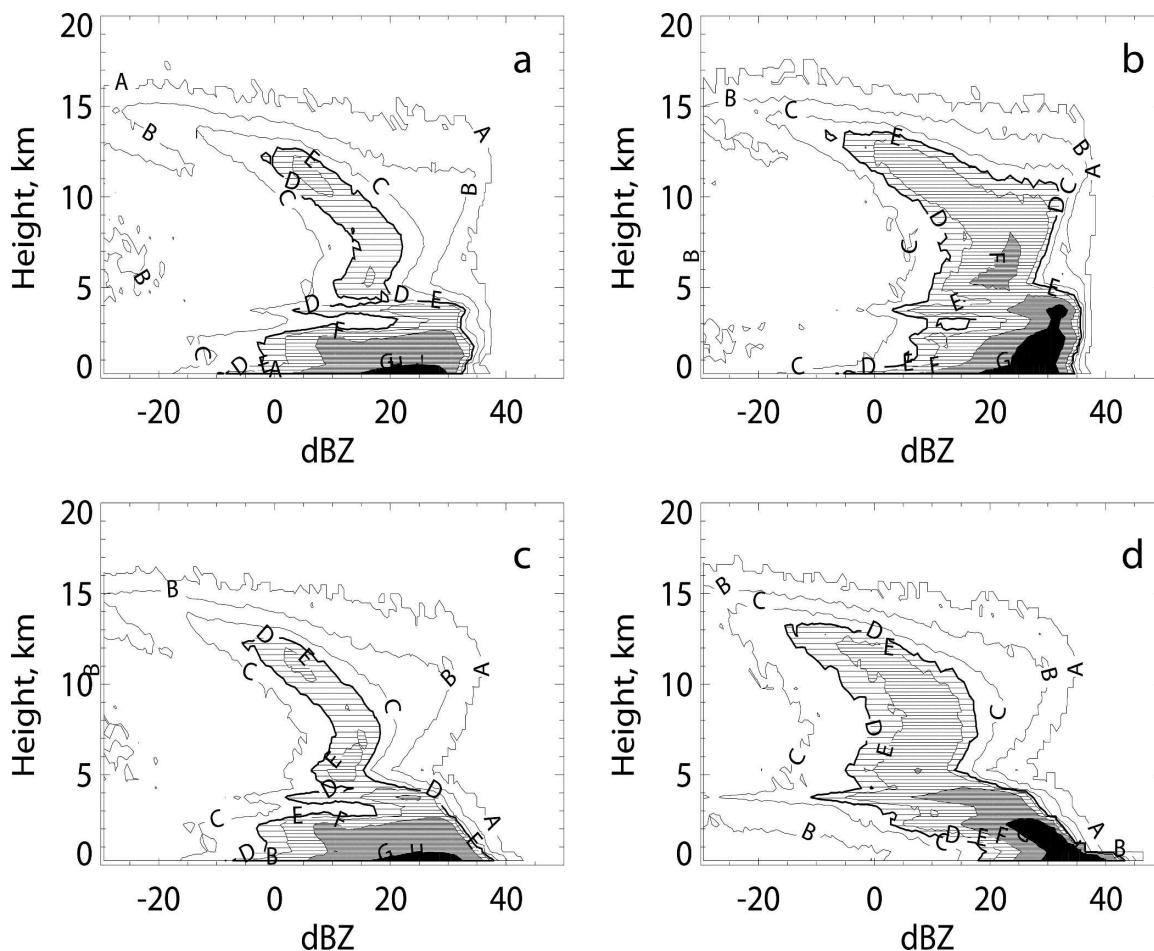
tenuation (e.g., Li et al. 2001; L'Ecuyer and Stephens 2002; Meneghini et al. 1983). Attenuation also represents a greater problem for interpreting MWR observations for radar systems operating at the ground than for interpreting observations from airborne radar or space-borne systems operating in a nadir-viewing mode since (i) the hard surface return observed in this latter mode provides a reference to determine the unambiguous presence of attenuation in a returned signal and (ii) the bulk of the attenuation occurs low in the atmosphere especially in convective systems where most of the liquid precipitation and vapor resides.

A sense of the differences in viewing convection from above versus below is provided in the work of Li et al. (2001) who matched surface MWR data [the Cloud Profiling Radar System (CPRS)] to the data collected from the overflight of an airborne MWR system [the Airborne Cloud Radar (ACR)] flown on the NASA DC-8 aircraft. Similar differences in observing convection from above with a nadir-viewing radar (referred to as space radar mode) in contrast to observations taken from below with a zenith-pointed radar (referred to as surface mode) are highlighted in Figs. 1 and 2. Shown is a collection of simulated Ka- and W-band radar reflectivity profiles composited into a cumulative frequency altitude display diagram (CFAD; e.g., Yuter and Houze 1995). These CFADs provide a convenient way of presenting the probability distribution of a large body of profiles of reflectivity. The simulated CFADs of Figs. 1 and 2 are created using cloud and precipitation condensate mixing ratios obtained from a cloud-resolving model configured in large-domain convective equilibrium experiments as described by Stephens et al. (2004). Figures 1 and 2 each contain four panels, two each for light rain defined as those profiles associated with surface rain rates in the range 10–30 mm day^{-1} and two each for heavy rain defined as those profiles associated with surface rain rates from 100 to 300 mm day^{-1}. The results emphasize the differences between viewing clouds from the bottom up compared to top down, especially at the higher frequency of the W band, which is subject to large amounts of attenuation in heavier precipitation. At the frequency of the Ka band, attenuation by heavy precipitation is discernible through the comparison of surface and space CFADs, the former showing a general shift (decrease) in reflectivities of about 10 dBZ above the model melting level (i.e., above about 5 km). By contrast, the W-band profiles for the light precipitation are similarly shifted by almost 10 dBZ. Heavy rain at this frequency attenuates the radar returns and compresses the surface observed profiles primarily to the rain layer below about 5 km with information above being lost. As noted later, the

FIG. 1. CFAD diagrams for Ka-band radar echos simulated from cloud-resolving model results. (a), (c) Model columns with light precipitation (10–30 mm day^{-1}) and (b), (d) with heavy precipitation (100–300 mm day^{-1}). (a), (b) Space-based radars and (c), (d) surface-based radars. Frequency contours represent counts normalized by the total number of radar profiles in the sample set. Frequency contours are A = 0.00002, B = 0.001, C = 0.005, D = 0.01, E = 0.015, F = 0.03, G = 0.1, H = 0.25, and I = 0.3. Heavier shading indicates increased frequency of occurrence.

frequency of occurrence of total attenuation of airborne W-band observations over the tropical convection observed during the Cirrus Regional Study of Tropical Anvils and Cirrus Layers–Florida Area Cirrus Experiment (CRYSTAL–FACE) experiment described below is less than 5%. The top-down view by contrast offers substantially more information in these heavy precipitation situations providing profiles that essentially extend through the entire troposphere.

3. Data sources

The amount of MWR data collected from different tropical locations has increased significantly over the last decade. MWRs were deployed by the ARM program at a number of tropical sites (see section 3c) making quasi-routine surface observations of tropical

cloudiness at these three sites. These MWR measurements are also made in conjunction with other measurement types, including surface precipitation, radiative fluxes, and routine soundings. MWRs have also been included as part of ship-borne sensor packages deployed in a number of observational experiments. In addition to these surface observations, a limited amount of W-band airborne radar data have also been collected over the past several years. Up to the time of the CRYSTAL–FACE experiment discussed below, none of these airborne data are of tropical convection. The experiments and measurement programs that supply the data analyzed in this paper are now briefly reviewed.

a. Joint Air–Sea Monsoon Interaction Experiment

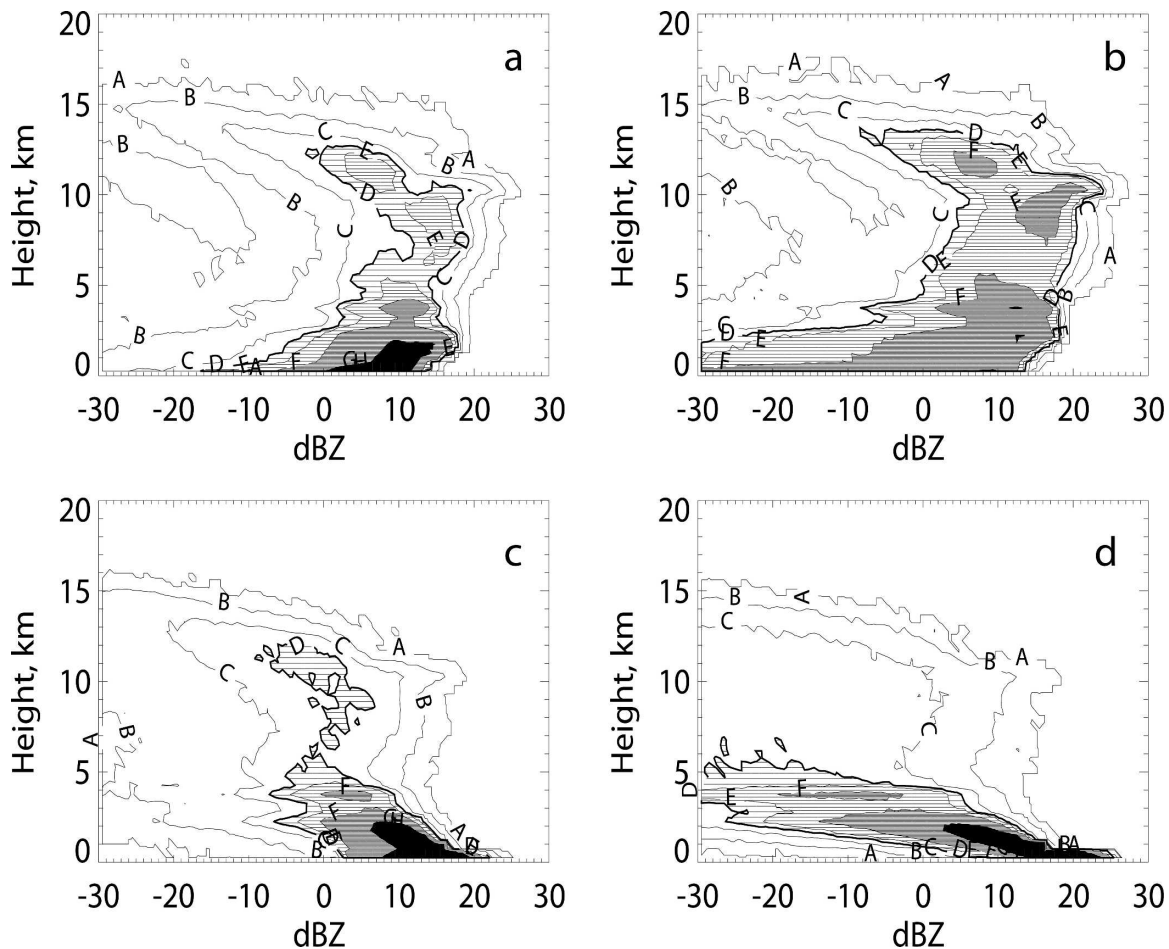The Joint Air–Sea Monsoon Interaction Experiment (JASMINE; Webster et al. 2002) was conducted in the

FIG. 2. Same as in Fig. 1, but these data represent simulated W-band radar echos.

eastern Indian Ocean and the southern Bay of Bengal during the summer of 1999. JASMINE sought to provide data on the upper Indian Ocean and atmosphere as a step toward observing coupled processes in the monsoon system. As summarized in Webster et al. (2002), an ensemble of in situ and remote sensing instruments were deployed to measure the ocean and atmosphere. A key platform during the April–June period of the experiment was the National Oceanic and Atmospheric Administration (NOAA) research ship *Ron Brown.* Included on this ship for observing the atmosphere were the NOAA/Environmental Technology Laboratory (ETL) Ka-band cloud radar, surface radiometers measuring solar and infrared fluxes, rawinsondes launched at 6-hourly intervals, rain gauge measurements, and other measures of bulk meteorology and surface fluxes.

During phase II of the observing period in May 1999, the sensors on the *Ron Brown* observed the monsoon oscillation with a quiescent period during the first half of the month followed by an active monsoon period

with associated large-scale outbreaks of deep convection. An example of 48 h of Ka-band radar data collected on 24 and 25 May 1999 during the period of monsoon outbreak is shown in Fig. 3. This diagram shows time–height cross sections of the MWR reflectivity and includes the matching time trace of precipitation. The 2 days highlighted are periods of persistent cloudiness with a large, deep convective complex observed over the ship for an almost 18-h period between 1200 UTC 24 May 1999 and 0600 UTC 26 May 1999. This period is followed by episodes of thick cloud above 5 km with underlying convection indicated by high reflectivity (above 10 dBZ) and recorded precipitation by the shipboard precipitation sensors. The cloud radar also shows evidence of total attenuation during the periods of heaviest rainfall typically at rates above about 5–10 mm h^{-1}, broadly confirming that predicted by L'Ecuyer and Stephens (2002). These periods of total attenuation are also highlighted in Fig. 3.

Table 1a summarizes the gross statistics of the MMCR profiles for both the entire period of JASMINE
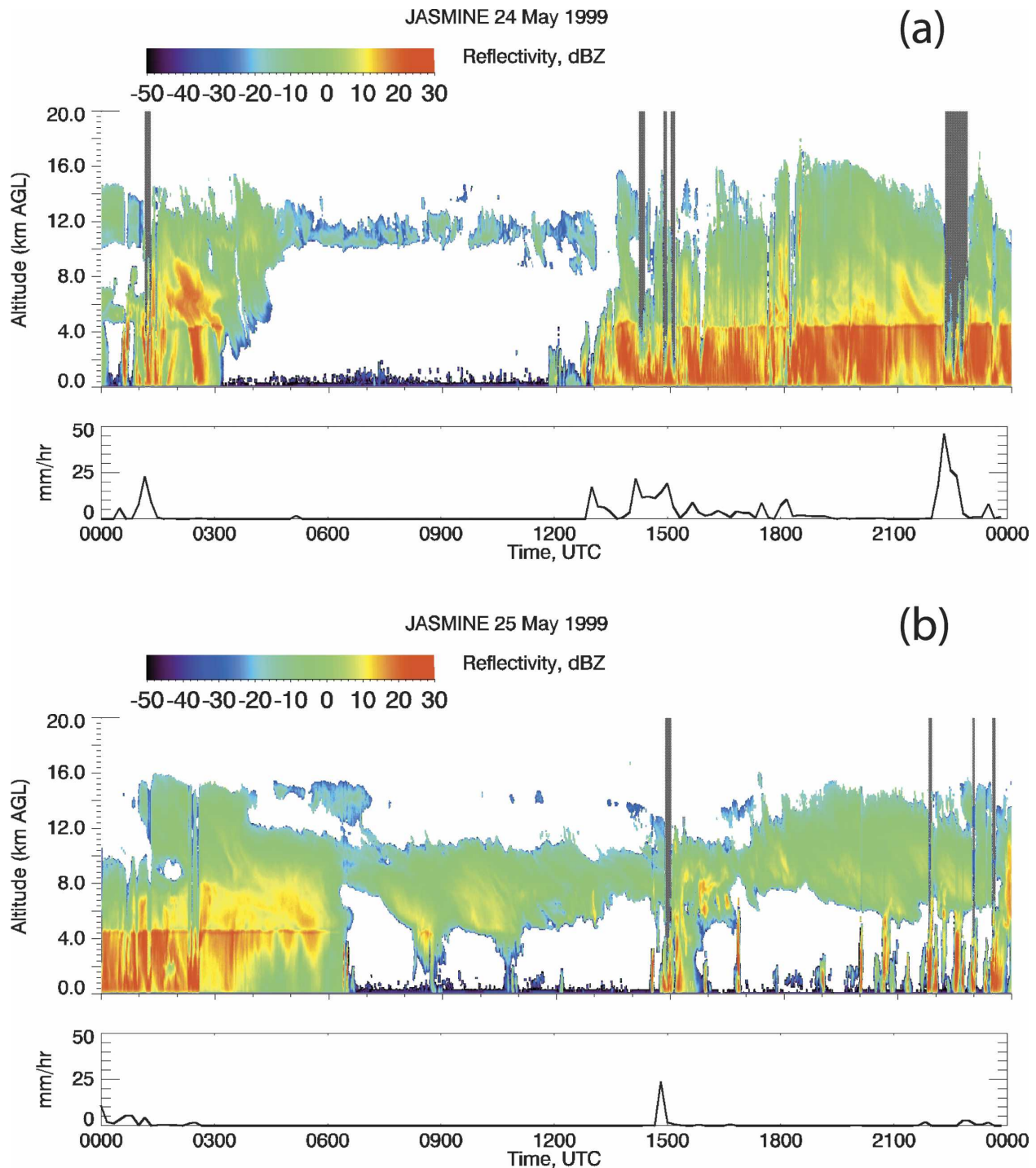
FIG. 3. Time–height cross section of MMCR profiles from JASMINE for (a) 24 May and (b) 25 May. Under each cross section is the corresponding trace of precipitation measurements from the rain gauge aboard the *Ron Brown*. Periods of attenuation are marked with gray shading.

and for two shorter periods identified as active and break periods of the monsoon. The table lists the total number of profiles, the fractions of these profiles deemed clear (no radar return), the fraction deter-mined as nominally cloudy without precipitation, and the fraction of precipitation producing clouds where the precipitation/no-precipitation profiles are identified ac-cording to the method described below. A number of

TABLE 1. Frequency of occurrence for profiles containing clear, CO, and precipitating columns for (a) JASMINE and (b) Manus.

(a)	JASMINE		
	All	Monsoon	Monsoon break
Tot days	27	5	6
Tot profiles	38 880	7200	8640
Clear	0.458	0.066	0.631
CO	0.444	0.593	0.355
Cloud with precipitation	0.098	0.340	0.014

(b)	Manus	
	MJO	Transition
Tot days	38	53
Tot profiles	328 320	457 920
Clear	0.110	0.436
CO	0.683	0.508
Cloud with precipitation	0.208	0.057

features of the convection stand out from these gross statistics. The five active monsoon days are exceptionally cloudy with only 7% of the profiles being clear, 59% contain clouds without precipitation, and 34% of the profiles contain precipitation. As expected, these fractions are very different for the monsoon break period with 63% of the profiles deemed clear and only 1% of the profiles containing precipitation.

b. CRYSTAL–FACE

In July 2002, the CRYSTAL–FACE (hereafter C–F) employed measurements from sensors on numerous aircraft, surface, and space-based platforms to study the life cycle of upper-tropospheric clouds (Jensen et al. 2004). NASA's *ER-2* aircraft carried a suite of sensors that replicate some aspects of the A-Train (e.g., Stephens et al. 2002 for a discussion of the A-Train). Included on this aircraft was the cloud physics lidar (CPL; McGill et al. 2002) and the inaugural flight of the 94-GHz Cloud Radar System (CRS; Li et al. 2004). This was the first time a MWR system was flown on a high-altitude aircraft platform capable of overflying tropical convection. The availability of matched ancillary information about convection such as from surface-based sensor systems deployed during C–F was unfortunately limited.

The convection observed during this experiment was frequently connected to diurnal sea-breeze activities although for a few days of the experiment convection also developed under the influence of large-scale ascent associated with the passage of easterly waves and other large-scale phenomena.

Figure 4 is an example of C–F radar data showing a time–height cross section of CRS radar reflectivity for a transect of the *ER-2* over convection that formed on 7 July. On that day, convection formed as the east and west coast sea breezes merged producing convection under the type-2 categorization of Blanchard and Lopez (1985). This merger produced an intense convective line evident in the Next Generation Weather Radar (NEXRAD) plan position indicator (PPI) image in Fig. 4c. The flight paths of the *ER-2* aircraft associated with the reflectivity cross section are superimposed on the Geostationary Operational Environmental Satellite (GOES) visible imagery from 1915 UTC. Data from a total of seven flight days are composited below for those portions of *ER-2* research flights that occurred over deep convection. As such these data are not a complete sample of all convective modes with occurrence statistics grossly skewed toward the deeper modes of convection. Nevertheless, of the 204 206 CRS profiles examined, only 4.7% of these suffered complete attenuation as determined by the lack of any surface return.

c. ARM

The U.S. DOE ARM contracted the NOAA/ETL to build a number of MWRs. A detailed description of these continuously operating autonomous systems developed for ARM is described in Moran et al. (1998). These MWRs operate at 34.86 GHz (8.7-mm wavelength) and are referred to as the MMCRs as previously noted. An MMCR has been operating essentially continuously at the ARM southern great Plains (SGP) site since late 1996, at the North Slope of Alaska site near Barrow since March 1998 and in the Tropics at Nauru and Manus since 1998 and 1999, respectively. An MMCR was also installed at Darwin, Australia, in 2002 but has operated there only intermittently.

The present study focuses on data collected from the Manus MMCR over a 3-month period from 1 December 2003 to 28 February 2004. Manus is located in the tropical western Pacific, at 2°S, 147.4°E. The context for these observations is provided in Figs. 5a,b each showing a Hovmöller diagram of satellite-observed outgoing longwave radiation (OLR). Figure 5a is derived for the latitude band 5°S–5°N stretched from 60°E to 120°W in longitude offering a broadscale view of two Madden–Julian oscillation (MJO) events, highlighted by the regions of OLR below 180 W m^{-2}. These events propagate across the domain dissipating near the date line. Figure 5b is a higher-resolution Hovmöller of IR brightness temperature confined to the longitudes of 120°–170°E for the single pixel at the latitude nearest the Manus ARM site. The location of Manus is indi-
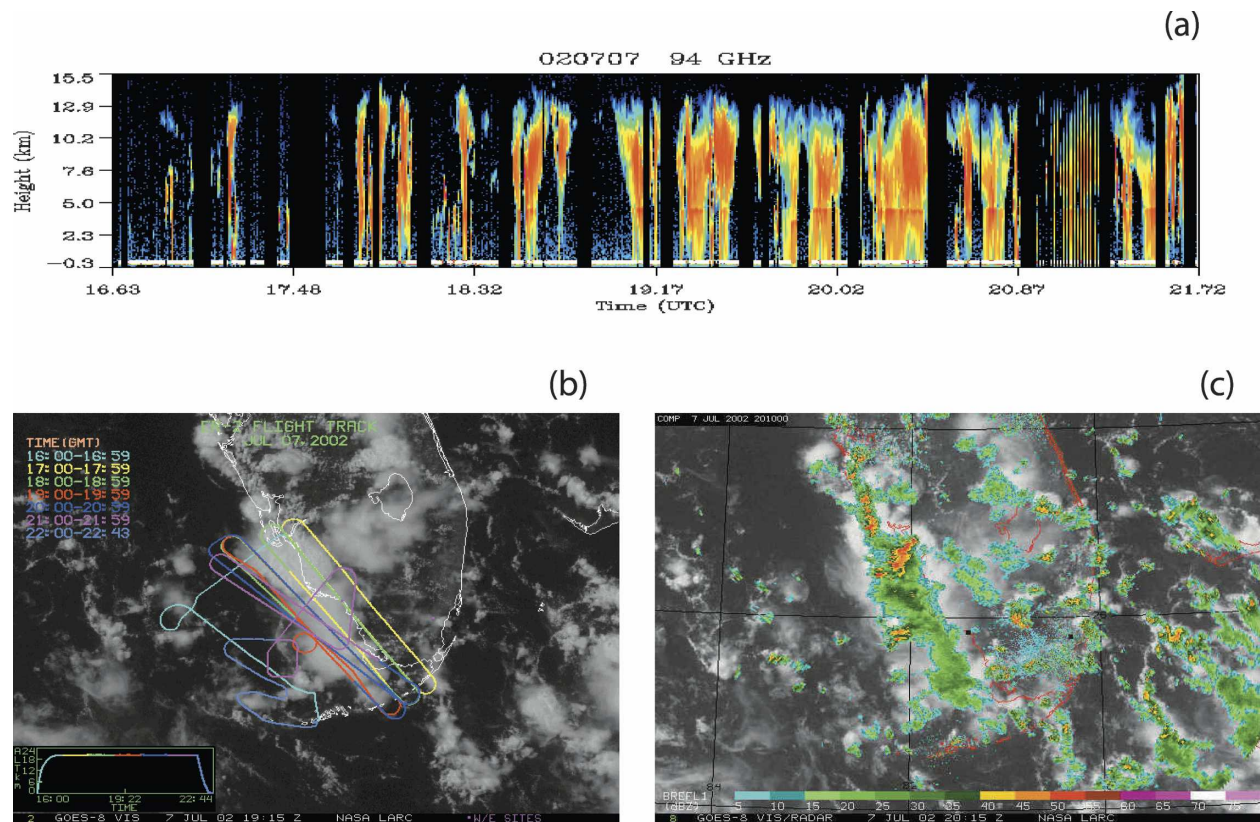
FIG. 4. (a) Time–height cross section of CRS profiles from CRYSTAL–FACE for 7 Jul 2002, (b) the corresponding flight tracks for the NASA *ER-2* superimposed on GOES visible imagery from 1915 UTC 7 Jul 2002, and (c) the corresponding NEXRAD PPI image for 2015 UTC 7 Jul 2002.

cated by the vertical line on this figure. The broad organization of the MJO apparent in Fig. 5a is also seen at the finer scale represented by Fig. 5b with the periods of most active deep convection mirroring those in Fig. 5a. This merely indicates that the convection observed at Manus at these times were indeed part of the larger-scale influence of the MJO. Another detail evident in Fig. 5b but smoothed in Fig. 5a, is the notable diurnal cycle of convection.

The MMCR observations are composited relative to the periods of active convection associated with the MJO and with respect to the transition periods between these convective outbreaks. Table 1b presents the general statistics of the total number of profiles analyzed for both periods noting the fractions of these profiles deemed clear (no radar return), the fraction determined as cloudy without precipitation and the fraction of precipitation-producing clouds. The active period of the MJO is very cloudy with only 11% of the profiles recorded as being clear in this period, 68% containing cloud without precipitation, and the remaining 21% of the profiles containing precipitation. As expected, these statistics differ for the transition phase with 44% of the profiles deemed clear, and only 6% containing precipitation.

4. Precipitation occurrence and MWR echoes

The analysis of MWR data reported in this paper requires an approach to determine the occurrence of precipitation. Profiles that are identified to contain significant precipitation are referred to as storm profiles and groups of like-profiles determined by the cluster analysis described in the next section identify storm classes. Here a simple procedure to identify precipitation in the profiles of reflectivity obtained from the surface-based Ka-band cloud radar is described and evaluated using the surface rain gauge measurements. The JASMINE radar profiles are reported at 1-min intervals, and the surface precipitation rates are reported as averages over 10-min intervals. The precipitation rate nearest in time to the radar profiles were correlated with the profiles in the evaluation (i.e., the measured precipitation within ± 5 min of a given radar profile). Precipitation accumulations were also computed as the measured precipitation rates weighted by the
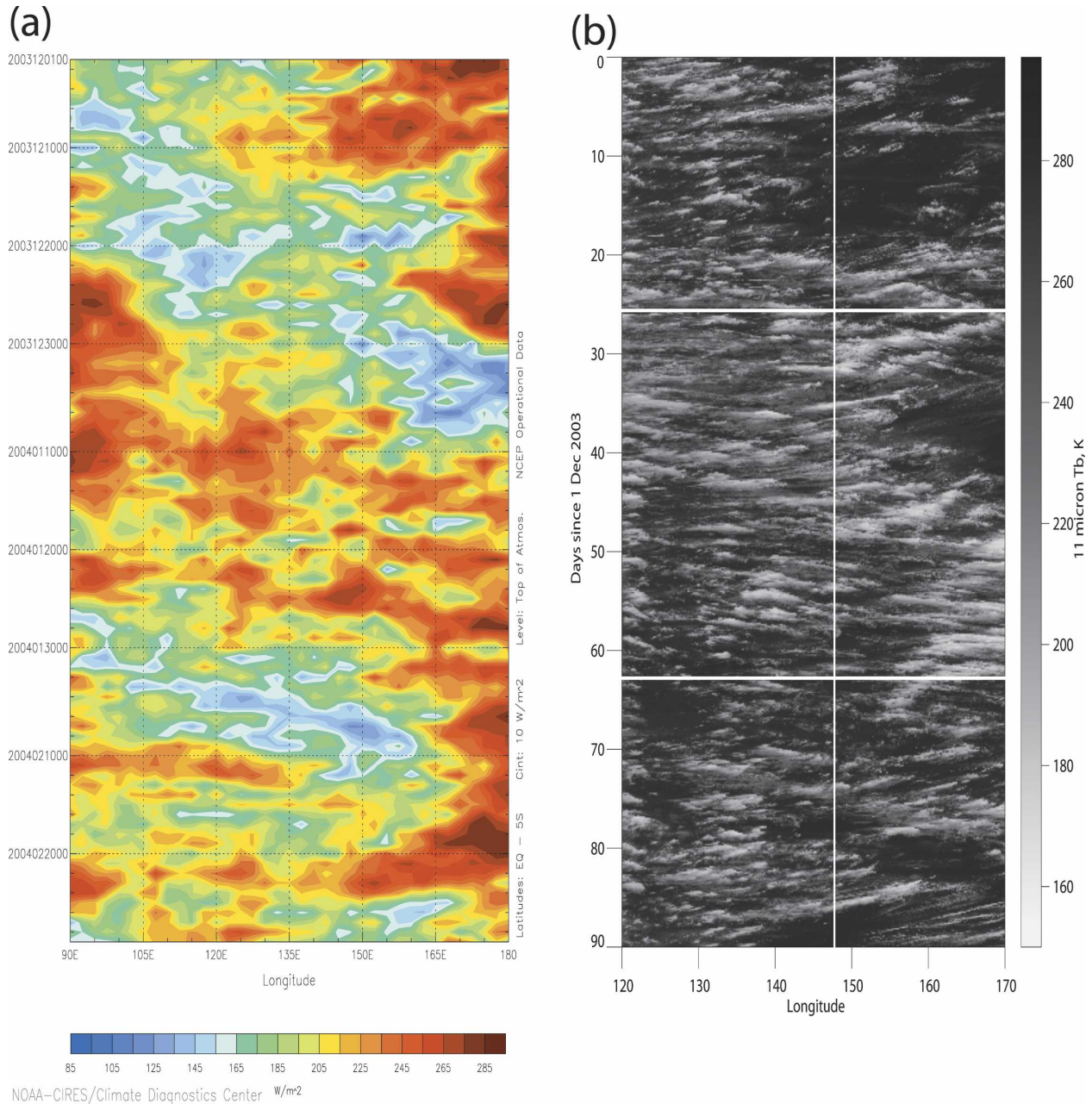
(a)

(b)

FIG. 5. (a) Hovmöller (time–longitude) diagram of daily mean OLR for the region bounded by 5°S and the equator for the period from 1 Dec 2003–28 Feb 2004. (Image provided by the NOAA–CIRES, Climate Diagnostics Center, from their Web site at http://www.cdc.noaa.gov.) (b) Hovmöller diagram of *GOES-9* 11-µm brightness temperature for the latitude nearest Manus at 2.0°S for the same period. The two horizontal lines indicate the approximate start (top line) and end (bottom line) of the active phase of the MJO. The vertical line indicates the approximate location of Manus at 147.5°E.

1-min radar profile interval and summed by storm class. A similar analysis was performed on the Manus radar data. In this case, the radar data are reported at 10-s intervals, whereas the precipitation is reported as an average precipitation rate over 1-min intervals. The precipitation rate observation nearest in time to any given radar profile (thus within ±30 s of the radar) was then assigned to that profile. The corresponding precipitation accumulation for a given profile was computed as precipitation rate multiplied by the 10-s radar profile interval and these accumulations were then summed for each storm class.

The method for flagging precipitation in the MWR profiles is based on correlative analysis of radar data

TABLE 2. Test results for the method for determining the presence of precipitation from the radar profile. Results represent tests on 555 317 radar profiles from JASMINE and Manus. Given that precipitation is predicted, the prediction is accurate 93.1% of the time.

Prediction result	Precipitation		No precipitation	
	Hit	Miss	Hit	Miss
Count	56 532	4160	407 917	86 708
Fraction	0.93	0.07	0.82	0.18

and coincident surface precipitation measurements. This analysis indicated that significant surface rainfall (above 0.1 mm h^{-1}) most commonly occurs when the lower contiguous 1-km layer of reflectivities exceeds -10 dBZ. The bulk statistics of such correlation, derived from analysis of 555 317 JASMINE and Manus cloudy profiles, are summarized in Table 2. This simple lower-layer reflectivity threshold approach identifies precipitation in 60 692 of these profiles. Approximately 93% of these profiles had recorded surface observations of precipitation. Approximately 83% of the total number of remaining profiles (i.e., 494 625 profiles) that were determined by this method to contain no precipitation also had no precipitation recorded at the surface. The majority of the designated nonprecipitation profiles remaining had only traces of light precipitation. Figure 6 provides a further perspective on this precipitation detection method. The figure presents the frequency of occurrence histograms of the measured surface precipitation for profiles from the Manus MJO period for which the method indicates no precipitation (top panel) and for which the method indicates precipitation (bottom panel). The top panel reflects the fact that the method predominantly misses the lighter rain and drizzle associated with precipitation rates primarily below 0.15 mm h^{-1}.

In presenting the storm analysis below, we use this -10 dBZ criteria to identify profiles containing precipitation and further use the maximum height of the 10-dBZ reflectivity in that profile as a proxy for the height of the precipitation. The latter was arrived at through some experimentation and is broadly analogous to the PR echo-top height (ETH) used in the analysis of the following section. Figure 7 provides a convenient summary of this simple classification. The first two groups of profiles are those that do not meet the -10 dBZ criterion, and these are hereafter designated as cloud only (CO) despite the fact that some fraction of them (19%, not shown) have (light) precipitation (averaging <0.2 mm h^{-1}) recorded at the surface. The two groups of profiles that meet the -10 dBZ criteria are further separated into a "drizzle" category (profiles for which
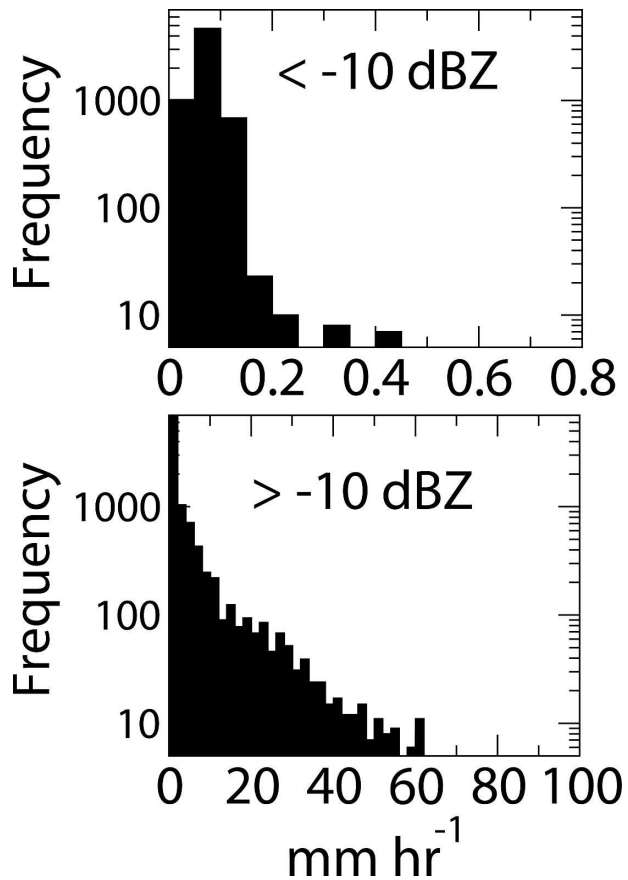

FIG. 6. Frequency histograms for Manus rain rates observed during the MJO periods between 1 Dec 2003 and 28 Feb 2004, segmented by the mean in-cloud reflectivity in the lowest kilometer of the atmosphere with (top) values less than -10 dBZ and (bottom) values greater than -10 dBZ.

reflectivities never exceed 10 dBZ) and a "storm" category (profiles for which reflectivities exceed 10 dBZ). The occurrence of the former is approximately 10% of all precipitation profiles (note the summations of the single and multiple drizzle occurrences in Table 3). The remaining category has no recorded reflectivity above -30 dBZ in a given profile and is thus deemed "clear." Figure 7 also provides the percentage occurrences of each of these classes derived from the entire dataset, indicating that 57% of the profiles fall into the CO class, 31% fall into clear and the remaining 12% contain (significant) precipitation.

Sampling issues are inherent in trying to examine advecting three-dimensional cloud and precipitation fields via measurements taken from fixed points on the surface. In particular, due to horizontal transport of hydrometeors, the possibility exists that surface precipitation measurements are slightly decoupled from the radar profiles. To some degree, this effect may be ame-

FIG. 7. Classification of radar profiles as "clear," "cloud only," "drizzle," or "storm" according to the occurrence of reflectivities Z_i at various thresholds, where Z_i is the radar reflectivity in dBZ at a particular radar range gate i, and the presence of a contiguous layer of reflectivities above or below -10 dBZ in the lowest kilometer of the profile.

liorated by the use of the time-averaged values for radar reflectivity and surface precipitation noted above. Additionally, the use of the lowest contiguous 1-km layer of reflectivities to identify precipitating columns serves to reduce the impact of this transport on the results presented here. These results should be considered applicable to the particular datasets examined, and it would be useful to evaluate these results using different sampling strategies.

5. Comparison to TRMM

NASA's TRMM was launched in late 1997 and has successfully accumulated more than 7 yr of PR data. Since the PR operates at a much longer wavelength (approximately 2 cm) than MWR systems, it suffers less from attenuation and "Mie effects" although the low sensitivity of the radar (approximately 18-dBZ minimum detectible signal) limits its usefulness for observing clouds and lighter precipitation.

The statistical properties of tropical convective precipitation observed by the TRMM PR have recently been conveniently summarized by Masunaga et al. (2005). Their study identified a number of distinct regimes of the convective precipitation and we show in Fig. 8 and the next section that the MWR reflectivities similarly differentiate these precipitation regimes as well as provide a more distinct view of the cloudiness associated with them.

Figure 8a is an example of the Masunaga et al. (2005) analysis of PR data matched to the 11-μm brightness temperatures of the VIRS instrument of TRMM. The results are presented in the form of the two-dimensional histogram of the frequency of occurrence of T_b and the maximum altitudes of the 18-dBZ radar echo heights. The histogram is a composite of May 1999 data obtained for the region of the Indian Ocean located in the rectangle defined by the coordinates 5°S–15°N and 88°–93°E. This time period coincides with an observational phase of the JASMINE experiment and the region encompasses the area of operation of the R/V *Ron Brown*.

Masunaga et al. (2005) subjectively define the five precipitation regimes indicated in Fig. 3a. For later, reference, the regimes noted (in color) are referred to as storm classes A–E noted on the diagram. Broadly, convective precipitation falls into one of two modes. One is shallow convection where PR maximum echo heights typically lie below the melting level occurring around 5 km. The second is a deeper mode of precipitation with maximum PR echo heights occurring mostly above the melting level. The analysis suggests that this deeper mode exhibits both a stratiform component and a deep convective component (e.g., Houze 1997). The 18-dBZ precipitation echo heights of the stratiform mode tend to be nearer the melting layer and are only marginally higher than the echoes of the shallow mode. The 11-μm cloud-top brightness temperatures, however, are cold with the implication that the precipitation falls from a deep layer of cloud characteristic of stratiform precipitation (e.g., Houze 1982).

Figure 8b presents the results of the application of a more objective cluster analysis approach to define the regimes of this diagram. In this case, the k-means cluster algorithm (Anderberg 1973) was applied to the same TRMM PR data used to produce Fig. 8a. These results were obtained by applying the k-means algorithm initiated with 12 centroid locations distributed regularly over the domain. The initial centroid locations were perturbed randomly using uniform distributions over ± 3 km for the precipitation echo-top height and over approximately ± 22 K for cloud-top brightness temperature. Two hundred repetitions were performed in which the k-means algorithm determined the best-fit final centroid locations. The resulting distribution of best-fit locations were then used to establish the precipitation echo-top height and cloud-top brightness temperature boundaries by which the storm classes were defined. These boundaries are used to classify each data point in the manner shown and identify the five main cluster types that closely relate to those of Masunaga et al. (2005). Also included in Fig. 8b is the relative frequency of occurrence of each storm class in the population. Figure 8c is the equivalent classification obtained from the application of the k-means algorithm to the MMCR observations obtained from the *Ron Brown* during the JASMINE experiment. The details of its construction are described in more detail in the

TABLE 3. Characteristics of single- and multilayered storm classes, showing for each the frequency of occurrence, total amount of associated precipitation, the relative fraction of the total precipitation, and the average precipitation rate. "JASMINE All" includes the complete 27 days of JASMINE data.

| | Manus MJO | | | | Manus transition | | | |
Storm class	Frequency	Tot precipitation (mm)	Precipitation fraction	Precipitation rate (mm h^{-1})	Frequency	Tot precipitation (mm)	Precipitation fraction	Precipitation rate (mm h^{-1})
A, single	0.012	21.3	0.033	10.69	0.007	2.78	0.016	5.75
A, multi	0.092	84.2	0.130	6.24	0.118	33.3	0.197	4.95
B, single	0.184	86.5	0.133	2.85	0.117	6.61	0.039	1.17
B, multi	0.208	107.1	0.165	3.30	0.125	21.0	0.124	3.20
C, single	0.196	32.1	0.049	1.21	0.161	8.46	0.050	1.28
C, multi	0.081	14.7	0.023	1.31	0.112	6.04	0.036	1.15
D, single	0.029	120.7	0.186	24.0	0.124	34.0	0.213	4.64
D, multi	0.020	88.0	0.136	23.8	0.049	36.0	0.202	11.07
E, single	0.038	46.5	0.072	7.59	0.048	10.06	0.060	4.20
E, multi	0.027	44.8	0.069	10.19	0.031	8.39	0.050	4.35
Drizzle, single	0.086	0.48	0.001	0.23	0.035	0.58	0.003	0.33
Drizzle, multi	0.026	2.78	0.004	0.40	0.073	1.41	0.008	0.52

| | JASMINE monsoon | | | | JASMINE all | | | |
Storm class	Frequency	Tot precipitation (mm)	Precipitation fraction	Precipitation rate (mm h^{-1})	Frequency	Tot precipitation (mm)	Precipitation fraction	Precipitation rate (mm h^{-1})
A, single	0.014	3.34	0.025	6.07	0.017	4.06	0.023	4.06
A, multi	0.065	22.4	0.166	8.43	0.078	25.2	0.140	6.14
B, single	0.217	18.2	0.135	2.05	0.170	20.5	0.114	1.95
B, multi	0.246	26.1	0.194	2.60	0.221	31.0	0.172	2.37
C, single	0.197	5.10	0.038	0.63	0.169	5.82	0.032	0.64
C, multi	0.138	5.58	0.041	0.99	0.122	7.38	0.041	1.07
D, single	0.034	26.2	0.195	19.20	0.061	39.9	0.221	12.53
D, multi	0.019	15.09	0.112	19.7	0.026	22.4	0.124	14.43
E, single	0.021	4.82	0.036	10.71	0.029	10.69	0.059	6.23
E, multi	0.018	6.56	0.049	13.12	0.034	11.54	0.064	5.92
Drizzle, single	0.006	0.005	0.000	0.02	0.025	0.47	0.003	0.50
Drizzle, multi	0.027	1.070	0.008	0.97	0.049	1.24	0.007	0.78

following section. The temperature scale used in this construction is simply the temperature that corresponds to the −30 dBZ echo-top height, which approximately corresponds to the cloud-top height and is used to facilitate comparison with the TRMM PR Visible and Infrared Scanner (VIRS) observations.

The differences between the physical −30 dBZ cloud-top temperature and the VIRS 11-μm brightness temperature are important for interpreting the differences in the frequency of occurrence of each class. Except for storm classes B and E, nominally considered the deep stratiform and congestus modes, respectively, the frequency of occurrence of the classes are similar implying that the MWR is capable of classifying convective precipitation in a manner almost identical to the TRMM Ku-band radar. As we will see later, however, differences in categories B and E between the TRMM data (Fig. 8b) and the MWR data (Fig. 8c) relate to the interpretation of the VIRS brightness temperature as

cloud top. In the case of TRMM data, cases of thin, transparent cirrus overlying the congestus mode are classified as congestus whereas the cloud radar −30 dBZ cloud-top temperature correctly identifies cloud top as high and cold and places these in category B. In the section to follow, we show that many of the storm class statistics are dominated by these multilayered systems and, even more surprisingly, that the accumulated precipitation from these same multilayered systems represent a significant fraction of the total precipitation.

6. Storm analysis

a. Histogram, and cluster analysis of storm regimes

The simple precipitation identification method discussed above was applied to all profiles to isolate the storm class profiles in the database. A classification of storm types analogous to those created from TRMM
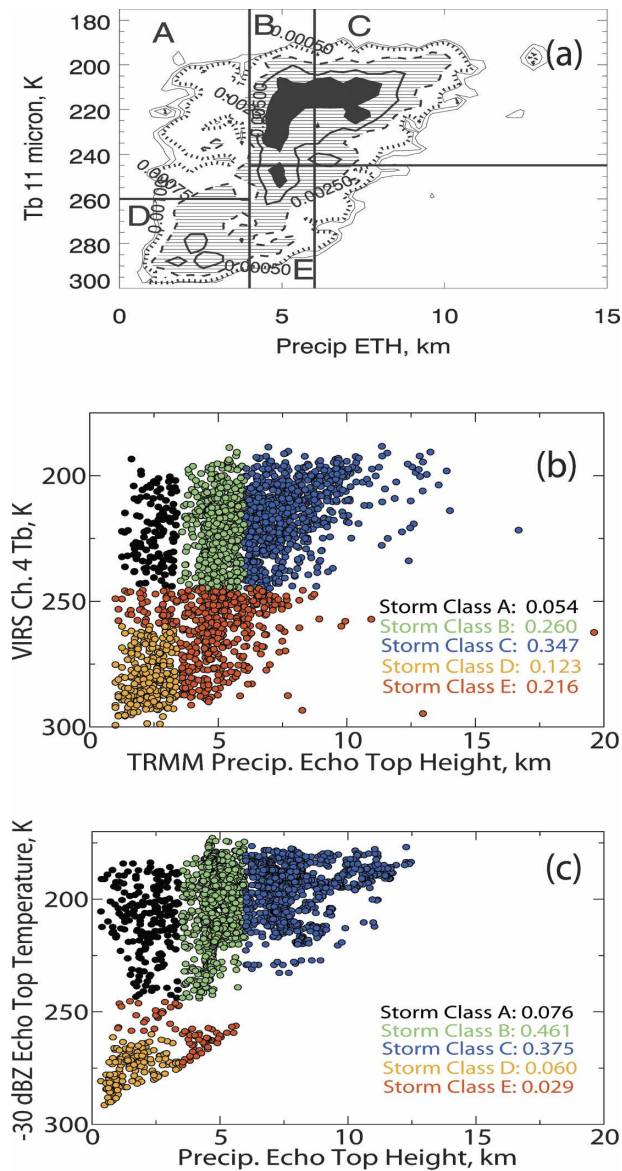
FIG. 8. Storm classes as defined (a) by Masunaga et al. (2005), applied to TRMM data from May 1999 over the JASMINE area of operation, (b) using the *k*-means technique applied to the same data, and (c) using the *k*-means technique applied to the May 1999 JASMINE MMCR profiles.

PR data (Figs. 8a,b) were then produced using these storm profiles from JASMINE, Manus, and from a composite of all seven C–F *ER-2* flights. The results of this classification are summarized in Figs. 9a–d. Each panel also provides the number of radar reflectivity profiles contained in the scatterplot and the relative frequency of occurrence of each storm type. Not shown is the JASMINE monsoon break scatterplot given it is constructed from a relatively small number of precipitating profiles. The number of total (cloud plus precipi-

tation) profiles estimated to suffer total attenuation was previously noted. In contrast to the classification of TRMM data shown in Figs. 8a,b, the maximum altitude of the −30 dBZ echo is used as a measure of the effective cloud-top height (y axis) and the maximum height of the 10-dBZ echo is also taken to be the precipitation ETH as previously mentioned. Significant attenuation by the heaviest precipitation introduces an obvious bias to the precipitation echo height derived from surface radars as was discussed previously. Thus attenuation tends to shift the precipitation ETH to lower levels than in reality biasing some fraction of the echoes of deep convective precipitation into the shallow regimes (i.e., into storm classes D and E), although this contamination is likely to occur in only a small fraction of all profiles for reasons noted.

The relative frequency of occurrence of the different storm classes summarized in Figs. 9a–d provides a gross indication of how tropical precipitation is organized. Convective outbreaks that occur during the active phases of the monsoon observed during JASMINE and the active phase of the MJO are dominated by classes C and B. The latter class represent a significant portion of the entire system occurring 44% and 48% of the time in the active MJO and monsoon periods, respectively. Storm classes of the MJO transition period are dominated by class C with the shallower convection (A + D + E) contributing about 30% of occurrence.

The general character of the cluster analysis of the C–F data shown in Fig. 9d is similar to those derived from the surface MWRs. However, the C–F data were conditionally sampled to include primarily deep convective complexes and consequently the relative frequency of occurrence of storm class C is considerably higher than that of the other data sources.

The implication of these statistics is that it is the implied deeper modes of convection (B + C) that is the most frequently occurring class of precipitation, either for the active (75% and 82%) or in break periods (57%) of tropical convection. However, it is shown below that the interpretation of storm C as deep convection and its related deep stratiform mode (class B), in particular, is misleading in the data analyzed. In fact the greatest frequency of occurrence and the largest accumulations of precipitation that appear in the data analyzed derive from multilayered cloud structures, typically involving shallower convection underlying upper layers of cirrus.

b. Storm class CFADs

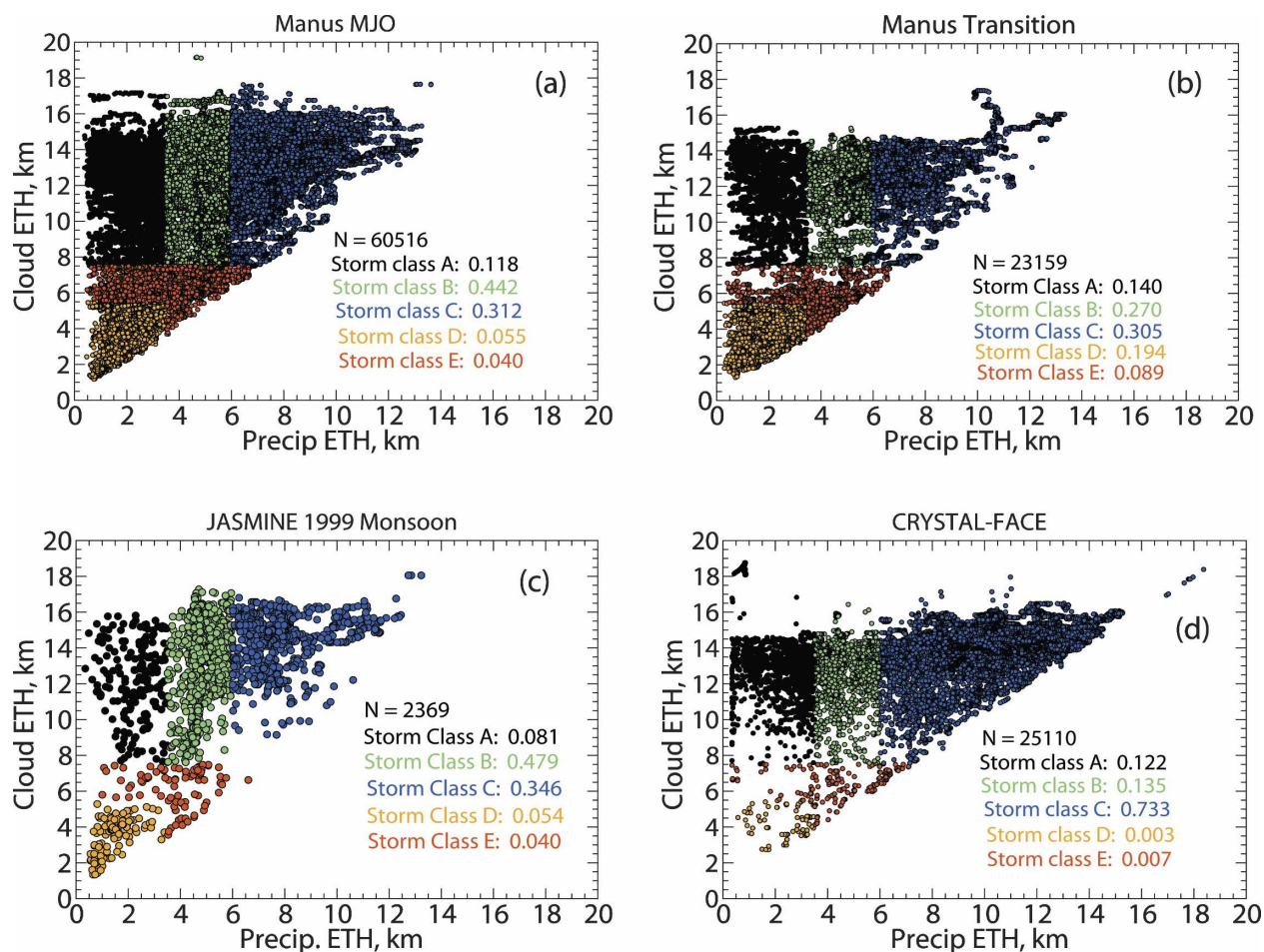The histogram results presented above connect cloud information in the form of −30 dBZ ETHs

FIG. 9. Storm classifications (derived from *k*-means analysis) applied to (a) Manus MJO, (b) Manus transition, (c) JASMINE monsoon, and (d) CRYSTAL–FACE radar estimates of cloud and precipitation ETHs. The relative frequencies of occurrence for the five storm classes are also shown in (a)–(d).

to precipitation echoes. This histogram analysis procedure, however, makes only minimal use of the information about the profiles of cloud and precipitation contained within the radar profiles. To illustrate the cloud structures associated with the different storm classes, Fig. 10 presents CFADs for the active period of the MJO at Manus. This figure is constructed from five panels of CFADs associated with each of the five storm classes (A–E) and a sixth panel that presents the CFADs derived from the nonprecipitating (CO) profiles observed during the same period. It is clear from the latter that the structure associated with nonprecipitating clouds is primarily cloudiness confined in the layer between approximately 10 and 15 km.

The bulk composites of Fig. 10 are informative providing broad characteristics of the depths of convection and cloud layers. However, the explicit vertical struc-

tures of the clouds associated with the different storm classes tends to be smeared out by compositing many profiles. To highlight the vertical structure, Fig. 11 presents two time–height cross sections of ARM MMCR reflectivities collected at Manus during the active period of the MJO. A typical mode of cloudiness revealed by visual study of such data is one of multilayered cloudiness with cumulus congestus–like convection underlying higher layers of cirrus as shown in this figure. Such systems occur within storm class B (and to a lesser extent C) and satellite observations of these classes can easily be misinterpreted as a deep stratiform mode of precipitation.

To separate the actual deeper modes of convection from these multilayered systems, an analysis was performed on all storm classes to identify the cloud layers and quantify the frequency of occurrence of multiple cloud layers in contrast to the occurrence of single lay-
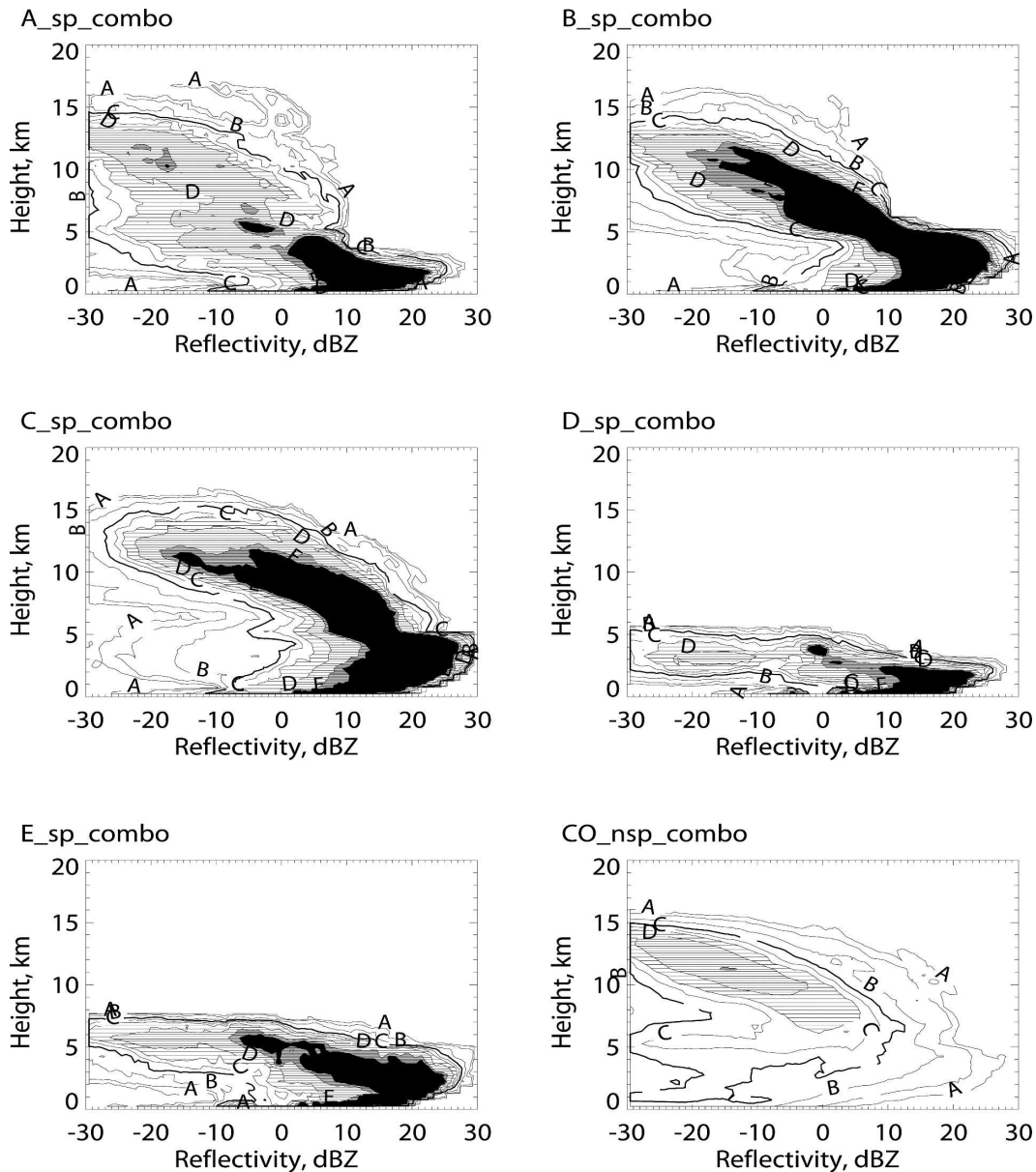
FIG. 10. CFADS from Manus MJO MMCR profiles for the five precipitating storm classes and for nonprecipitating (CO) profiles. Normalized frequencies are shown as in Fig. 1. Frequency contours are as follows (labels for alternating contours are in parentheses): 0.005 (A), 0.01, 0.025 (B), 0.005, 0.075 (C), 0.1, 0.15 (D), 0.25, 0.3 (E) and 0.5. Heavier shading indicates increased frequency of occurrence.

ered profiles.[2] Multilayer clouds were discerned by counting the number of cloud-free to cloudy transitions in the radar profiles, progressing from the top of the

profile to the ground. The statistics of this analysis are summarized in Table 3 in the form of the fractional frequency of occurrence statistics of single versus multiple modes of cloudiness for each of the five storm classes plus the additional drizzle class. Table 3 also provides the associated precipitation accumulated over the entire observing period and the fraction of this accumulated precipitation associated with each class (including the drizzle class) as well as the average rate of

---

[2] To evaluate the extent to which our conclusions about multi-layered clouds might be dependent on this cloud layer identification procedure, we developed an entirely different and more elaborate method for identifying cloud layers. When applied to the data, the same cloud layer statistics were obtained.
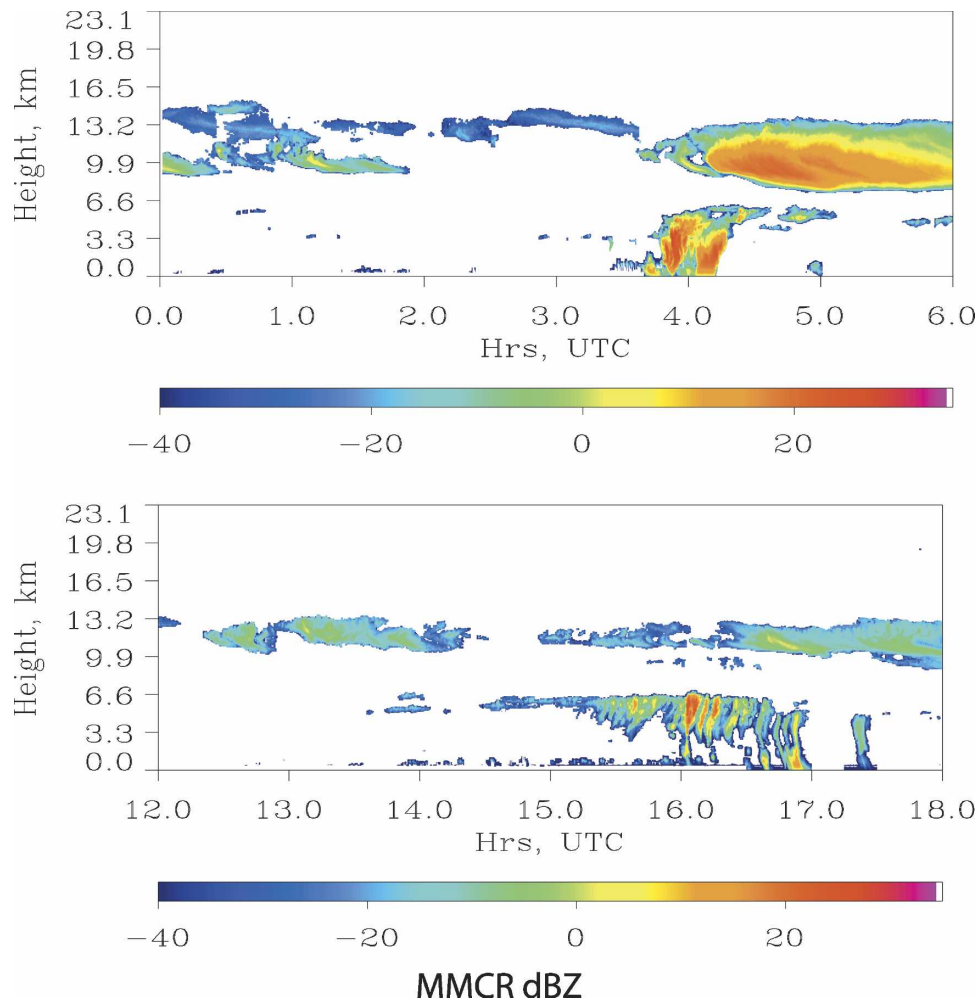
FIG. 11. Representative time–height cross sections of Manus MJO MMCR radar profiles, illustrating instances of congestus underlying cirrus.

precipitation. The statistics are provided for the Manus MJO active and transition and the JASMINE active monsoon and the combination of active and break (all JASMINE) observing periods.

Table 4 summarizes the results of Table 3 showing the relative frequency of occurrence of multilayered systems and the fractional contribution to the total accumulated water that falls from all classes of storms (including drizzle) summed over all observing periods. These statistics reveal that the occurrence of multiple layered systems ranges from 45% to 53% of all classes and are the dominant mode of class B. For example, the fractional occurrence of multilayered systems is 0.25 versus 0.22 for single layered systems for class B of the monsoon and 0.21 and 0.18, respectively, for the active periods of the MJO. Furthermore, 57% of the observed accumulated precipitation that fell during the monsoon

period of JASMINE, 53% of the precipitation that fell during the MJO active period, and 63% of all the precipitation that fell during the MJO transition period were associated with these multilayered systems.

Another feature of the cloud structures associated with each storm class is demonstrated through the CFAD pattern correlation statistics summarized in Table 5. This table summarizes the pattern correlations calculated using two-dimensional cross correlation. The table lists the maximum correlation coefficients of the CFAD structures of the active phase of the MJO correlated with the CFADs for the same classes obtained for the JASMINE monsoon and MJO transition observing periods. Also listed are the reflectivity and height offsets that produce the maximum pattern correlations. All values of correlation lie above 0.7 with the majority of values exceeding 0.8 suggesting that the

TABLE 4. Summary of single- and multilayered class statistics, showing for each the frequency of occurrence, total amount of associated precipitation, and the relative fraction of the total precipitation.

Storm class	Manus MJO			Manus transition		
	Frequency	Tot precipitation (mm)	Precipitation fraction	Frequency	Tot precipitation (mm)	Precipitation fraction
Single	0.546	307.0	0.474	0.493	62.5	0.371
Multi	0.454	342.0	0.526	0.507	106.1	0.629
Storm class	JASMINE monsoon			JASMINE all		
	Frequency	Tot precipitation (mm)	Precipitation fraction	Frequency	Tot precipitation (mm)	Precipitation fraction
Single	0.489	57.7	0.429	0.470	81.4	0.452
Multi	0.512	76.8	0.571	0.530	98.7	0.548

CFAD structures of each respective storm class of the three weather regimes studied (i.e., the regimes of the active and transition phases of the MJO and the active period of the monsoon) are essentially the same and that the main differences between the convection of these weather regimes is the relative frequency of occurrences of each class.

Figure 12 provides insight on the structure of these multilayered systems for storm classes A, B, and C. The figure summarizes the structure showing both CFADs and histogram statistics on the number of layers, cloud-top heights, and layer thicknesses derived from Manus data of the MJO. The picture that emerges is that the multilayered systems are most frequently in the form of two layers, one being high with tops above about 12 km. The second precipitating layer lies below this layer of upper-level cloudiness with tops typically slightly above the melting level.

7. Other surface properties

The collocation of other surface measurements with the surface radar observations available both from the ARM program and in the JASMINE experiment provide the opportunity to examine the properties of these measurements grouped according to the convective storm classes. Each of the radar profiles, categorized by storm class, was matched to coincident surface observations of downwelling long- and shortwave fluxes, and surface precipitation. As mentioned previously, the MMCR profiles are recorded at 10-s intervals at Manus, while surface meteorology and radiative flux measurements are recorded as 1-min averages. Surface data within the 1-min window bracketing the time of the radar profile were considered here as coincident. The radar profiles of JASMINE, are reported at 1-min intervals and the surface observations are 10-min averages. The surface data within the 10-min window brack-

eting the radar profile were then matched and accumulated to produce the statistics summarized in Figs. 13, 14, and 15.

The measured quantities presented in Figs. 13, 14, and 15, respectively, are the downward longwave fluxes, surface precipitation, and an effective column solar transmittance. The latter is derived as a ratio of the measured fluxes to the clear-sky fluxes matched in time where the clear-sky fluxes are determined from a composite of clear-sky observations collected during the experiment. This transmittance quantity provides a convenient relative measure of transmittance across the different classes as well as a convenient way of normalizing the bulk effects of solar zenith angle on the transmittance. The rain-rate quantity of a particular storm class was obtained from the accumulated rainfall converted to rain rate based on the accumulated duration of the precipitation. The measurements are summarized for each storm class (A–E) including the additional drizzle and CO classes and are presented in the

TABLE 5. Two-dimension cross-correlation coefficients between storm class CFADS for Manus MJO and both the JASMINE monsoon and Manus transition. The terms (xx, yy) are the reflectivity (xx) and height (yy) offsets that produce the maximum correlations.

| Correlations vs Manus MJO	JASMINE monsoon	Manus transition
Storm class A, single	0.705 (0.0, 0.0)	0.790 (0.0, 0.0)
Storm class A, multi	0.789 (0.0, 0.0)	0.961 (0.0, 0.0)
Storm class B, single	0.891 (0.0, 0.5)	0.911 (0.0, 0.0)
Storm class B, multi	0.877 (0.0, 0.5)	0.929 (0.0, 0.0)
Storm class C, single	0.853 (0.0, 0.0)	0.917 (0.0, 0.0)
Storm class C, multi	0.842 (0.0, 0.0)	0.927 (0.0, 0.0)
Storm class D, single	0.761 (0.0, 0.5)	0.896 (0.0, 0.0)
Storm class D, multi	0.737 (0.0, 0.5)	0.885 (0.0, 0.0)
Storm class E, single	0.761 (0.0, 0.5)	0.880 (0.0, 0.0)
Storm class E, multi	0.744 (0.0, 0.5)	0.827 (0.0, 0.0)
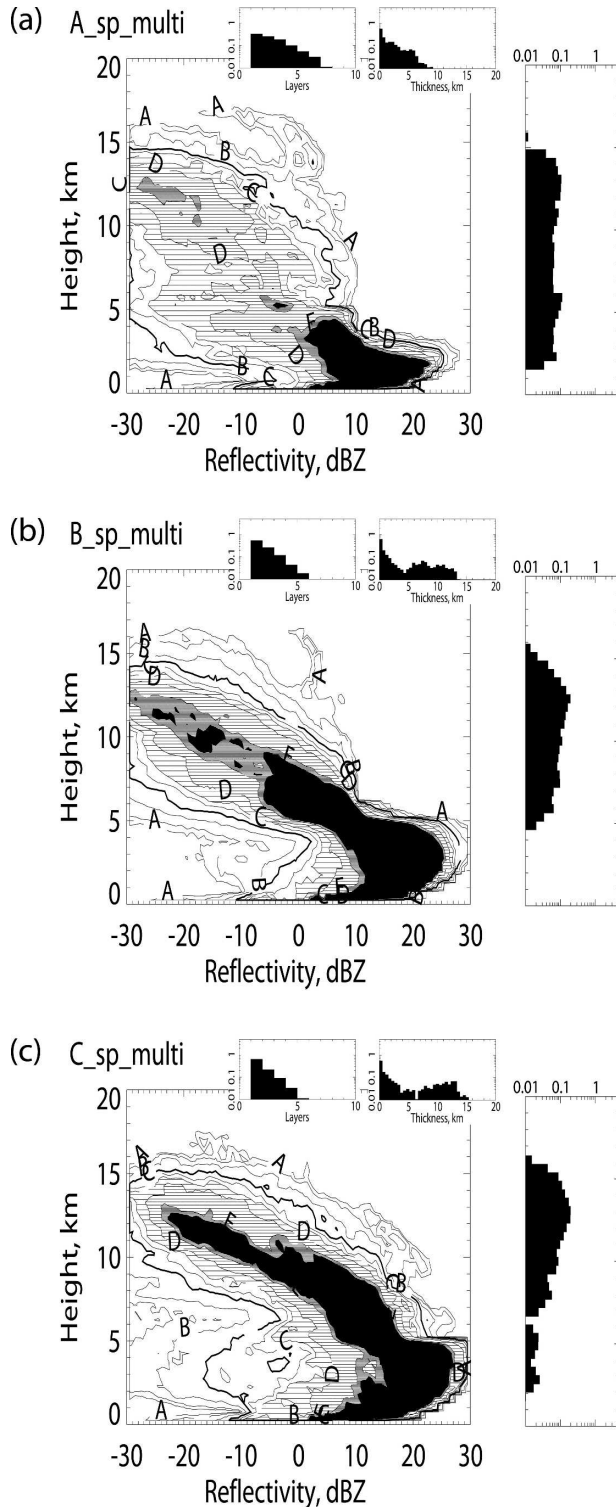
FIG. 12. CFADS for multilayer forms of storm classes A, B, and C. To the right of the CFADS are plotted histograms showing the normalized frequencies of occurrence of layer cloud-top heights. Above the CFADS are plotted histograms showing the normalized frequencies of occurrence for (left) number of layers and (right) layer thickness. Frequency scales on histograms are logarithmic. CFAD normalized frequencies, contour values, and shading are the same as in Fig. 10.

form of box-whisker plots. The statistics are reported as percentiles, with the lower and upper whiskers showing the 5th and 95th percentile values, respectively. Similarly, the lower and upper box edges indicate the 25th and 75th percentiles, and the midbox the 50th percentile. Figures 16a,b provide a clearer view of the class-to-class variability showing the differences in the 50th percentile values of clear minus cloudy longwave fluxes (Fig. 16a) and the CO minus storm class solar transmittances (Fig. 16b) with near-dawn and near-dusk cases removed.

The main results gleaned from these figures are as follows:

(i) The surface longwave fluxes only vary by about 10 W m^{-2} between storm classes A–E and D (as judged from the variations relative to clear-sky values of the 50th percentile values of fluxes). The variability within each class (as judged by the range of the 25th–75th percentile) is also about 10 W m^{-2} (Fig. 13a). Furthermore, the longwave fluxes associated with precipitating convection (A–E) are about 20–30 W m^{-2} larger than the related clear-sky fluxes. The longwave fluxes associated with the CO class are more similar to the clear-sky fluxes differing only from the clear sky by about 5–20 W m^{-2}. This general behavior of these longwave fluxes and the modest variability of the fluxes is a consequence of the characteristically large column water vapor amounts typical of the atmosphere observed at that time of the radar measurements.

(ii) The precipitation rate varies considerably across the storm classes with the maximum tending to be associated with the nominally shallow storm classes D and E reflecting the effects of attenuation and the misclassification of deeper convection into these classes. The precipitation rates are also not substantially different between the single and multilevel storm groups.

(iii) The solar transmittances reveal that significantly less sunlight reaches the surface in the precipitating regimes than reaches the surface under either the drizzle or CO conditions (Fig. 14b). These reductions are about 30%–50% of the CO transmittances. This result implies that the optical thicknesses of precipitating clouds significantly exceed those of nonprecipitating clouds. The variability of transmission, as judged by the range of the 25th–75th percentile, is also largest for the drizzle and CO cases. There is not an obvious difference in transmission properties of single versus multilayered classes.
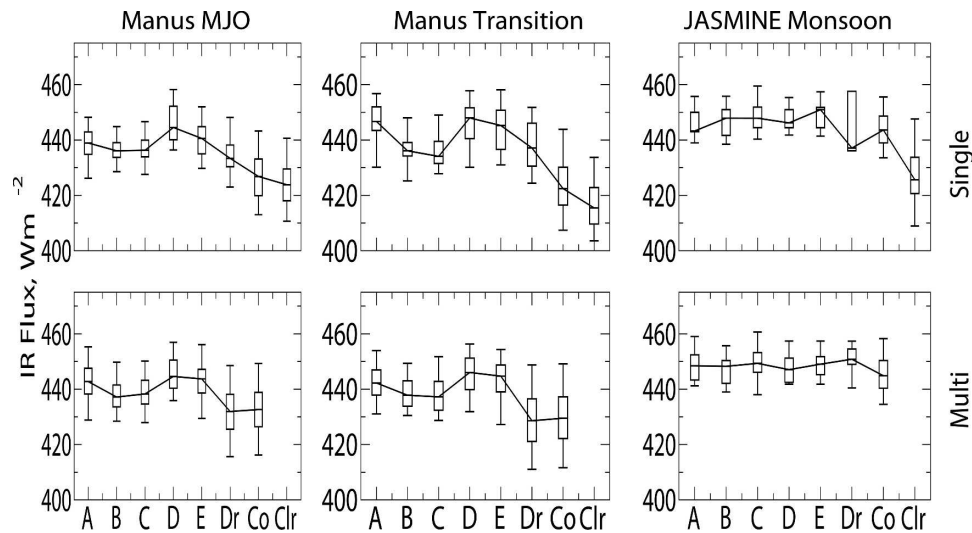
FIG. 13. Characteristics of the downwelling infrared radiative flux at the surface as a function of stormclass for Manus MJO, Manus Transition, and JASMINE Monsoon. Box centers mark the 50th percentile values, box bottoms and tops mark the 25th and 75th percentile values, respectively, and lower and upper whiskers mark the 5th and 95th percentile values, respectively.

8. Discussion and summary

This study provides analysis of over 825 000 profiles of millimeter-wave radar reflectivities primarily collected by zenith-pointing surface radars observing tropical convection associated with various phases of activity of the large-scale tropical circulation. The data principally analyzed in this paper come from surface observations obtained at the ARM Manus site during active and break episodes of the Madden–Julian oscillation (MJO) and from observations collected from a ship-borne radar during an active phase of the monsoon over the Indian Ocean during the JASMINE experiment. The study underscores the value of such millimeter-wave radar observations for studying tropical convection, and its associated cloudiness and precipitation structures.

The principal findings of the paper are as follows.

(i) A histogram regime analysis of precipitation echo heights and proxies for cloud-top heights reveal structures in the data suggestive of different con-
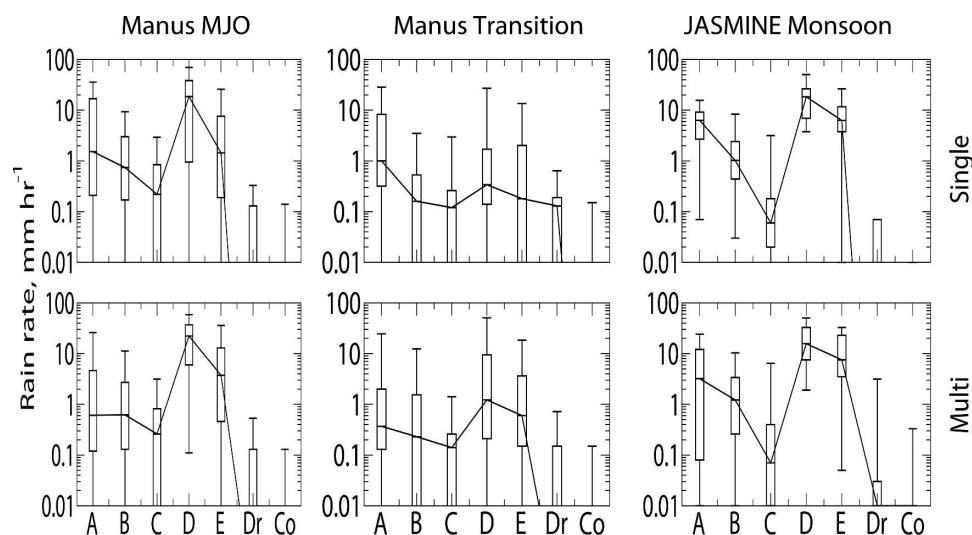

FIG. 14. Same as in Fig. 13, but for rain rate. The vertical coordinate has been scaled logarithmically, in order to accomodate the range in values.

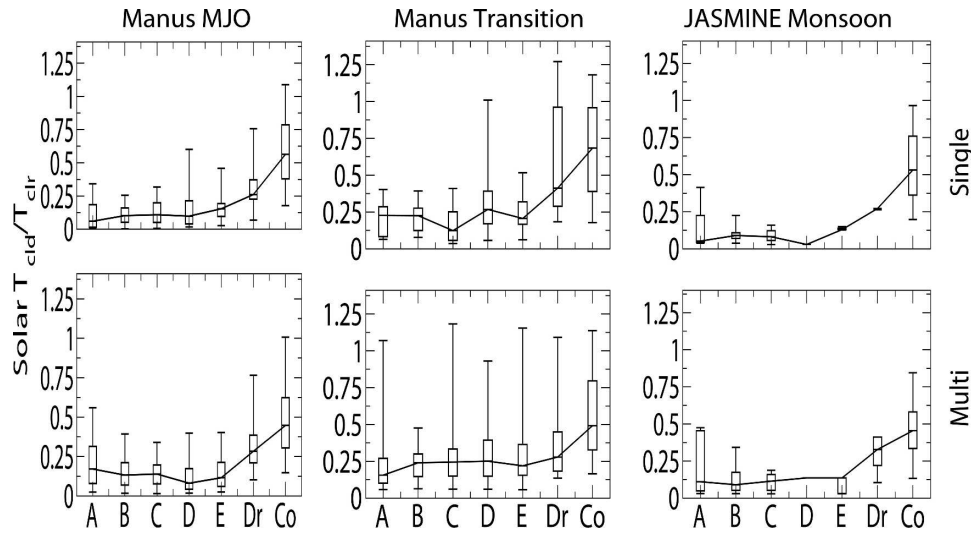Manus MJO Manus Transition JASMINE Monsoon

FIG. 15. Same as in Fig. 13, but for effective column solar transmittance (as defined in the text).

vective precipitation regimes. When these regimes are derived from surface MWR Ka-band measurements they produce regime occurrences that are similar in most respects to TRMM observations. Attenuation of the surface MWRs by heavy precipitation, however, leads to a misclassification of deeper precipitation modes into the shallow modes of precipitation. The extent of this misclassification cannot be fully quantified given the ambiguity in detecting the existence of total attenuation. It is relevant to note, however, that the frequency of occurrence of total attenuation in nadir-viewing W-band radar observations of tropical convection was only 5% of the profiles collected over deep convection during the entire CRYSTAL–FACE experiment. This misclassification is also less of an issue for nadir-pointing radars such as those flown on high-altitude aircrafts or on satellites.

(ii) The cloud and precipitation structures of the different precipitation regimes identified in the analysis were largely identical regardless of the mode of synoptic forcing, that is regardless of whether the convection occurred during an active phase of the MJO, a transition phase of the MJO, or in an active monsoon period. CFAD pattern correlations typically exceed 0.8. What changes between these synoptically forced modes of convection are the relative frequencies of occurrences of the different storm regimes (Fig. 9) and not the regimes themselves.

(iii) A surprising result that emerged from the analysis of the study was that the cloud structures associated with the majority of cases of observed pre-

cipitation (ranging from 45% to 53% of all precipitation-connected radar reflectivity profiles) indicated multilayered structures regardless of the mode of synoptic forcing. The predominant multi-
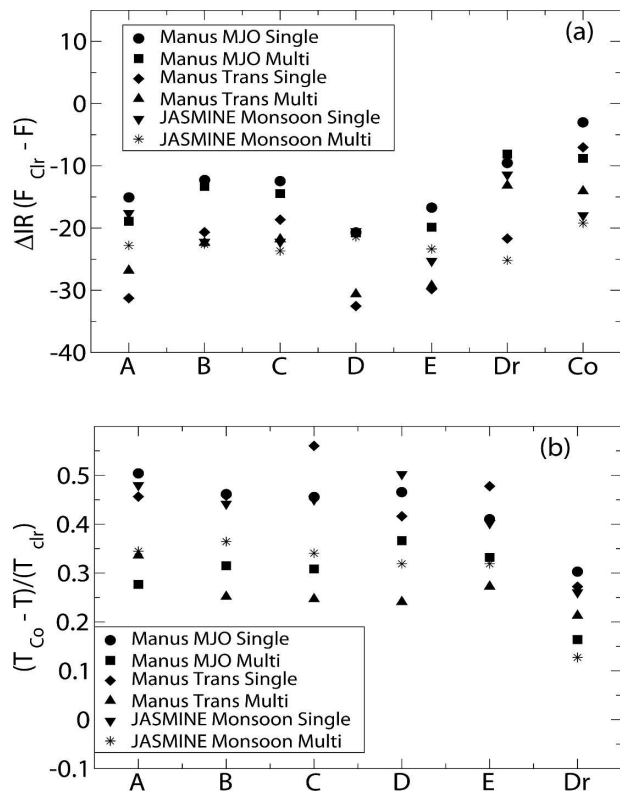

FIG. 16. Differences in 50th percentile values of (a) downwelling longwave fluxes for all storm, drizzle (Dr), and cloud-only (CO) profiles vs clear-sky profiles and (b) effective column solar transmittance for all storm and drizzle profiles vs CO profiles.

layered cloud mode was of higher-level cirrus of varying thickness overlying cumulus congestus–like convection below. This convection typically reaches to or slightly above the melting level. When viewed from above with a passive suite of satellite sensors, or even with the combination of passive VIRS and PR data of TRMM, these modes are easily misinterpreted as deep stratiform (e.g., Masunaga et al. 2005) or missed entirely being placed, for example, in the cirrostratus category of the International Satellite Cloud Climatology Project (ISCCP).

(iv) Even more surprising is the finding that the rain rates are not significantly lower in the multiple-layered systems than in the single deeper systems (Fig. 13b). Furthermore, the majority of water accumulated (i.e., 53%–62%) over each of the periods assigned to the active monsoon (5 days of data), the active MJO (38 days of data), and the transition MJO (53 days of data) fell from these multiple-layered cloud systems.

(v) Surface longwave fluxes vary modestly across the different types of convection due to the governing effects of large water vapor overburdens. The fluxes vary by about 10 W m^{-2} between and within storm classes A–E and differ by about 20–30 W m^{-2} from the clear-sky measurements. The solar transmittances, by contrast, reveal that significantly less sunlight (reductions of about 30%–50%) reaches the surface in the precipitating regimes than reaches the surface under drizzle and cloud only conditions, suggesting that the optical thicknesses of precipitating-bearing clouds significantly exceeds those of nonprecipitating clouds.

The analysis reported in this paper applies to a limited dataset and the representativeness of the results to the broader Tropics cannot be assessed at this time. The extent that these findings are reproduced in the global observations of CloudSat is thus of some interest. Should these results prove to be robust and the multi-layered statistics of cloudiness and convection of this study prove representative of the global Tropics, then the implications of the findings are likely to be substantial. Specifically, the study would suggest that a shallow mode of heating, largely ignored, appears to be important mode of atmospheric heating. Further study is also needed to determine the more intimate relation and phasing of the shallower modes of convection and their related precipitation to the deeper convective regimes. These issues, and others, are to be addressed in future studies.

REFERENCES

Anderberg, M. R., 1973: *Cluster Analysis for Applications*. Academic Press, 359 pp.

Arakawa, A., 2004: The cumulus parameterization problem: Past, present, and future. *J. Climate,* **17,** 2493–2525.

Austin, R., and G. L. Stephens, 2001: Retrieval of status cloud microphysical parameters using millimetric radar and visible optical depth in preparation for CloudSat. Part I: Algorithm formulation. *J. Geophys. Res.,* **106,** 28 233–28 242.

Benedetti, A., G. L. Stephens, and J. M. Haynes, 2003a: Ice cloud microphysics retrievals from millimeter radar and visible optical depth using an estimation theory approach. *J. Geophys. Res.,* **108,** 4335, doi:10.1029/2002JD002693.

——, ——, and T. Vukicevic, 2003b: Variational assimilation of radar reflectivities in a cirrus model. Part I: Model description and adjoint sensitivity studies. *Quart. J. Roy. Meteor. Soc.,* **129,** 277–300.

Blanchard, D. O., and R. E. Lopez, 1985: Spatial patterns of convection in south Florida. *Mon. Wea. Rev.,* **113,** 1282–1299.

Bretherton, C. S., and Coauthors, 2004: The EPIC 2001 stratocumulus study. *Bull. Amer. Meteor. Soc.,* **85,** 967–977.

Bony, S., and K. Emanuel, 2001: A parameterization of the cloudiness associated with cumulus convection; Evaluation using TOGA COARE data. *J. Atmos. Sci.,* **58,** 3158–3183.

Clothiaux, E. E., M. A. Miller, B. A. Albrecht, T. P. Ackerman, J. Verlinde, D. M. Babb, R. M. Peters, and W. J. Syrett, 1995: An evaluation of a 94-GHz radar for remote sensing of cloud properties. *J. Atmos. Oceanic Technol.,* **12,** 201–229.

Del Genio, A., W. Kovari, M.-S. Yao, and J. Jonas, 2005: Cumulus microphysics and climate sensitivity. *J. Climate,* **18,** 2376–2387.

Emanuel, K., and M. Zivkovic-Rothman, 1999: Development and evaluation of a convection scheme for use in climate models. *J. Atmos. Sci.,* **56,** 1766–1782.

Frisch, A. S., C. W. Fairall, and J. B. Snider, 1995: Measurement of stratus cloud and drizzle parameters in ASTEX with Ka-band Doppler radar and microwave radiometer. *J. Atmos. Sci.,* **52,** 2788–2799.

Houze, R. A., Jr., 1982: Cloud clusters and large-scale vertical motions in the tropics. *J. Meteor. Soc. Japan,* **60,** 396–410.

——, 1997: Stratiform precipitation in regions of convection: A meteorological paradox? *Bull. Amer. Meteor. Soc.,* **78,** 2179–2196.

Jensen, E. J., D. Starr, and O. Toon, 2004: Mission investigates tropical clouds. *Eos, Trans. Amer. Geophys. Union,* **85,** 45–50.

Johnson, R. H., 1995: Observations for validating cumulus parameterizations. *Proc. ECMWF Seminar, Parameterization of*

Sub-Grid Scale Physical Processes, Reading, United Kingdom, ECMWF, 55–75.

Kollias, P., R. Lhermitte, and B. A. Albrecht, 1999: Vertical air motion and raindrop size distributions in convective systems using a 94 GHz radar. *Geophys. Res. Lett.,* **26,** 3109–3112.

——, B. A. Albrecht, and F. D. Marks Jr., 2003: Cloud radar observations of vertical drafts and microphysics in convective rain. *J. Geophys. Res.,* **108,** 4053, doi:10.1029/2001JD002033.

Kropfli, R. A., and Coauthors, 1995: Cloud physics studies with 8 mm wavelength radar. *Atmos. Res.,* **35,** 299–313.

Kummerow, C., and Coauthors, 2000: The status of the Tropical Rainfall Measuring Mission (TRMM) after two years in orbit. *J. Appl. Meteor.,* **39,** 1965–1982.

L'Ecuyer, T. S., and G. L. Stephens, 2002: An estimation-based precipitation algorithm for attenuating radars. *J. Appl. Meteor.,* **41,** 272–285.

Lhermitte, R., 1988: Observations of rain at vertical incidence with a 94 GHz Doppler radar: An insight of Mie scattering. *Geophys. Res. Lett.,* **15,** 1125–1128.

Li, L., and Coauthors, 2001: Retrieval of atmospheric attenuation using combined ground-based and airborne 95 GHz cloud radar measurements. *J. Atmos. Oceanic Technol.,* **18,** 1345–1353.

——, G. M. Heymsfield, P. E. Racette, L. Tian, and E. Zenker, 2004: The 94 GHz cloud radar system on a NASA *ER-2* aircraft. *J. Atmos. Oceanic Technol.,* **21,** 1378–1388.

Liao, L., and K. Sassen, 1994: Investigation of relationships between Ka-band radar reflectivity and ice and liquid water contents. *Atmos. Res.,* **34,** 231–248.

Mace, G. G., T. P. Ackerman, E. E. Clothiaux, and B. A. Albrecht, 1997: A study of composite cirrus morphology using data from a 94-GHz radar and correlations with temperature and large-scale vertical motion. *J. Geophys. Res.,* **102,** 13 581–13 593.

——, ——, P. Minnis, and D. F. Young, 1998: Cirrus layer microphysical properties derived from surface-based millimeter radar and infrared interferometer data. *J. Geophys. Res.,* **103,** 23 207–23 216.

Masunaga, H., T. L'Ecuyer, and C. D. Kummerow, 2005: Variability in the characteristics of tropical precipitation systems. Part I: Spatial structure. *J. Climate,* **18,** 823–840.

Matrosov, S. Y., 1999: Retrievals of vertical profiles of ice cloud microphysics from radar and IR measurements using tuned regressions between reflectivity and cloud parameters. *J. Geophys. Res.,* **104,** 16 741–16 753.

——, 2005: Attenuation-based estimates of ranfall rates aloft with vertically pointing Ka-band radars. *J. Atmos. Oceanic Technol.,* **22,** 43–54.

McGill, M. J., D. L. Hlavka, W. D. Hart, V. S. Scott, J. D. Spinhirne, and B. Schmid, 2002: Cloud physics lidar: Instrument description and initial measurement results. *Appl. Opt.,* **41,** 3725–3734.

Meneghini, R., J. Eckerman, and D. Atlas, 1983: Determination of the rain rate from a spaceborne radar using measurements of total attenuation. *IEEE Trans. Geosci. Remote Sens.,* **21,** 34–43.

Moran, K. P., B. E. Martner, M. J. Post, R. A. Kropfli, D. C. Welsh, and K. B. Widener, 1998: An unattended cloud-profiling radar for use in climate research. *Bull. Amer. Meteor. Soc.,* **79,** 443–455.

Randall, D. A., M. Khairoutdinov, A. Arakawa, and W. Grabowski, 2003: Breaking the cloud parameterization deadlock. *Bull. Amer. Meteor. Soc.,* **84,** 1547–1564.

Redelsperger, J.-L., and Coauthors, 2000: A GCSS model intercomparison for a tropical squall line observed during TOGA-COARE. Part I: Cloud-resolving models. *Quart. J. Roy. Meteor. Soc.,* **126,** 823–863.

Stephens, G. L., 1994: *Remote Sensing of the Lower Troposphere.* Oxford University Press, 523 pp.

——, 2005: Cloud feedback in the climate system: A critical review. *J. Climate,* **18,** 237–273.

——, and Coauthors, 2002: The CloudSat mission and the A-TRAIN: A new dimension to space-based observations of clouds and precipitation. *Bull. Amer. Meteor. Soc.,* **83,** 1771–1790.

——, N. B. Wood, and L. A. Pakula, 2004: On the radiative effects of dust on tropical convection. *Geophys. Res. Lett.,* **31,** L23112, doi:10.1029/2004GL021342.

Stevens, B., and Coauthors, 2003: Dynamics and Chemistry of Marine Stratocumulus—DYCOMS-II. *Bull. Amer. Meteor. Soc.,* **84,** 579–593.

Webster, P. J., and Coauthors, 2002: The JASMINE pilot study. *Bull. Amer. Meteor. Soc.,* **83,** 1603–1630.

Yao, M.-S., and A. Del Genio, 1999: Effects of cloud parameterization on the simulation of climate changes in the GISS GCM. *J. Climate,* **12,** 761–779.

Yuter, S. E., and R. A. Houze, 1995: Three-dimensional kinematic and microphysical evolution of Florida cumulonimbus. Part II: Frequency distributions of vertical velocity, reflectivity, and differential reflectivity. *Mon. Wea. Rev.,* **123,** 1941–1962.